Increased power output of an electromagnetic vibration energy harvester through anti-phase resonance.

Faruq Muhammad Foong[1], Thein Chung Ket*[,1], Ooi Beng Lee[2], Daniil Yurchenko[3]

[1]School of Engineering and Physical Sciences, Heriot-Watt University, No. 1, Jalan Venna P5/2, Precinct 5, 62200 Malaysia
[2]Intel PSG, PG 14, Plot 6, Bayan Lepas Technoplex, Medan Bayan Lepas, 11900 Penang, Malaysia
[3] School of Engineering and Physical Sciences, Heriot-Watt University, Edinburgh EH14 4AS, United Kingdom
*c.thein@hw.ac.uk

Abstract

This paper proposes a novel method to increase the power output of a cantilever beam-based electromagnetic vibration energy harvester through anti-phase resonance. A new cantilever beam design is presented to achieve this. By introducing an anti-phase motion between the coil and the magnets at resonance under the same base excitation input, the relative velocity of the coil cutting through the magnetic field is significantly increased and hence its power output. An experiment is performed to compare the proposed method with the conventional method where either the coil or the magnet is fixed onto the vibrating base. Under a base acceleration level of 0.10 g and a natural frequency of 17.24 Hz, results shows a 185% increase in power for the proposed method when compared with the conventional method with a recorded maximum power of 7.4 mW at resonance. The power produced by this method is proven to be higher than the sum of power produced by two individual conventional harvesters under the same velocities. In addition, a 22% increase in frequency bandwidth is also recorded by the proposed method. In terms of the power density, the proposed method indicates a 38% increase when compared with the conventional harvester. Results also show a drastic reduction in the maximum power output and phase difference when the natural frequencies of the coil and the magnets differ by only 1.5%, hence defining the importance of frequency matching. Further analysis indicates that a glass fiber cantilever beam showed a higher decrease in electromagnetic damping as compared to the increase in mechanical damping when small bulk masses were added onto the beam, hence increasing its overall gain.

Keywords: Vibration energy harvesting, Out-of-phase, Resonance, Cantilever beam, Power.

1. Introduction

1.1 Literature review

Over the past decade, advancement in wireless sensor network (WSN) technologies have allowed the development of low powered WSN [1]. Currently, most WSNs are still powered by conventional batteries, which has the disadvantages of a large volume, limited power supply and high maintenance cost. Hence, research in energy harvesting towards finding a sustainable source of power for WSN became increasingly popular [2–4]. One of the most promising source of energy that was initially proposed by William and Yates [5] is vibrations. Vibration energy harvesting emerged as an encouraging energy source due to its high power density in terms of electrical conversion and its abundance from the surrounding [6]. Many transduction methods exist to convert mechanical vibration energy into electrical power, with the two most common methods being piezoelectric conversion and electromagnetism. Piezoelectric conversion method demonstrated a higher power density at small volumes whereas electromagnetic conversion is more favourable when space is not a constraint [7]. However, Beeby et al. [8] showed that the power density of an optimized electromagnetic vibration energy harvester can surpass the power density of a piezoelectric harvester, even at small volumes.

Various researches have been conducted throughout the past decade to increase the power output and the frequency bandwidth of a vibration energy harvester. Thein et al. [9] performed a finite element optimization algorithm to determine the optimum topology for a piezoelectric vibration energy harvester that would result in the maximum power output. Similarly, Chen et al. [10] also conducted a topology analysis to determine which shape between rectangular, trapezoidal and triangular cantilever beam would result in the highest power output of a piezoelectric harvester. Ooi and Gilbert [11] proposed a dual-resonator design consisting of two cantilever beams facing each other, where a pair of magnets is attached to one beam and a coil is attached to the other. It was shown that under dissimilar resonant frequencies, the bandwidth between the two resonant frequencies was improved due to the effect of superposition. However, the maximum power recorded did not exceed the individual power outputs

of both beams. Cottone et al. [12] proposed a technique to increase the power output of an electromagnetic vibration energy harvester through the concept of velocity amplification. By using multiple masses and springs, a 33 times increase in power gain was obtained when compared with a single mass configuration. Several researches have also explored the effect of a hybrid energy harvester in where the piezoelectric and electromagnetism transduction method was combined into a single harvester [13–15]. While an increase in power output was observed, the recorded power output was less than the sum of the power outputs from the two individual transduction methods.

The concept of anti-phase vibration have been explored by several researchers as an option to increase the power output of a vibration energy harvester. Kim et al. [16] performed a theoretical analysis on a two-degree-of-freedom bi-stable energy harvester composed of two piezoelectric cantilever beams. It was concluded that when the two beams are out-of-phase from each other, they exhibit a double well dynamic motion. Ando et al. [17] applied the concept of bi-stable parallel beams with tip magnets to achieve anti-phase motion. As a result, a ten time increase in power output from the two piezoelectric beams were recorded when compared with a single beam. However, it may be difficult to apply this concept for an electromagnetic harvester's design as anti-phase motion would also be desired for the coil. In a study made using dielectric elastomers in vibration energy harvesting, the design proposed by Yurchenko et al. [18,19] showed that the best voltage output was achieved from the anti-phase motion of the ball and the cylinder. Lee and Chung [20] applied the concept of anti-phase motion in a pendulum-based electromagnetic energy harvester and recorded a 37% increase in power when compared to a single-phase pendulum.

Despite the various power amplification solutions presented in past literatures, there have yet been a study that emphasises on an anti-phase motion at resonance for cantilever beam-based electromagnetic harvesters. The concept of anti-phase resonance may prove to be beneficial in terms of electromagnetic power output due to the increase in relative velocity. In this work, a method to increase the power output of an electromagnetic vibration energy harvester through anti-phase resonance was proposed. The idea was to maximise the relative velocity of the coil cutting through the magnetic flux of two permanent magnets by making the coil and the magnet vibrate out-of-phase from each other at resonance under the same base excitation input. Based on Faraday's law of electromagnetism, this will result in a significant increase in power output. The results from the proposed method were analysed and compared to the results of a conventional method in where the coil was fixed onto the vibrating base. Additionally, the effect of the phase difference on the power output of the anti-phase resonance method and the effect of the effective mass on the gain of an electromagnetic energy harvester were also studied.

1.2. Design of anti-phase resonance electromagnetic vibration energy harvester

To achieve anti-phase motion at resonance, a new cantilever beam design was presented as seen in Figure 1.

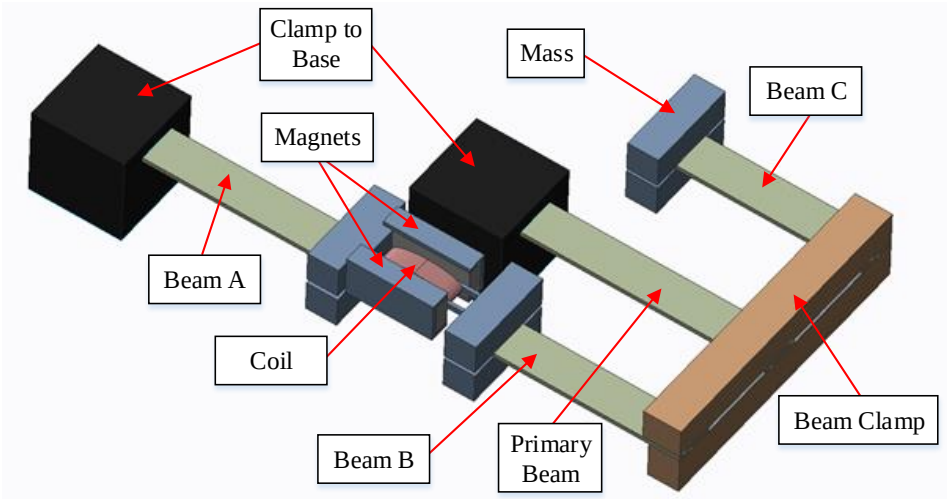

Figure 1. Anti-phase cantilever beam-based electromagnetic vibration energy harvester design.

The design consist of two smaller beams (beam B and beam C) that are clamped to one end of a primary cantilever beam. The other end of the primary beam is clamped to a vibrating base. When the primary beam vibrates, the free-end of the primary beam would experience a maximum deflection and hence creating a significant amplitude gradient

at this location. This will cause beams B and C to deflect in the opposite direction from the free-end primary beam. Figure 2 provides a visual aid of the side view as to how the design would vibrate. The coil was modelled as a block mass for simplicity. It can be seen that when the free-end of the primary beam deflect downwards, beams B and C would deflect upwards. Conversely, beams B and C would deflect downwards when the free-end of the primary beam deflects upwards.

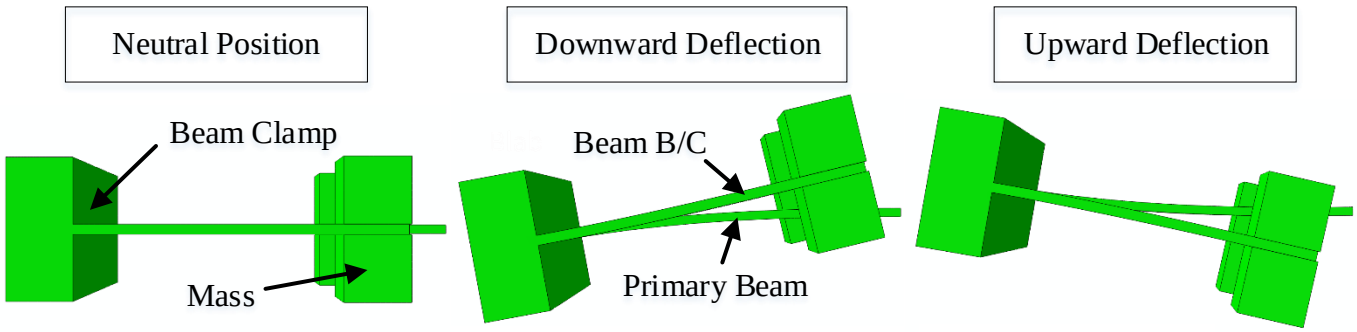

Figure 2. Visualised motion of the proposed anti-phase resonance design.

The new beam design must be paired with at least one individual cantilever beam (beam A) to generate power. A coil was attached to beam B and a pair of magnets is fixed onto beam A. A mass was added onto the other smaller beam to ensure a balanced mass. An unbalanced mass would result in a non-linear motion for beams B and C in where the beam with the larger inertial effect would vibrate stronger, causing rotation or twisting on the horizontal axis of the primary beam. This in turn would cause a non-linear phase change in the design making it harder to achieve the designs maximum potential. In addition, the induced rotation can also lead to physical contact between the coil and the magnets which can retard their motion. It is worth to note that it is possible to replace the mass with another coil. However, in this work, it was sufficient to analyse only one side due to symmetry in the design.

2. Derivation of governing equations.

2.1 Equation of motion for beam A

Consider a case where a lumped mass is placed on top of the free-end tip of a clamp-free cantilever beam under harmonic base excitation as shown in Figure 3.

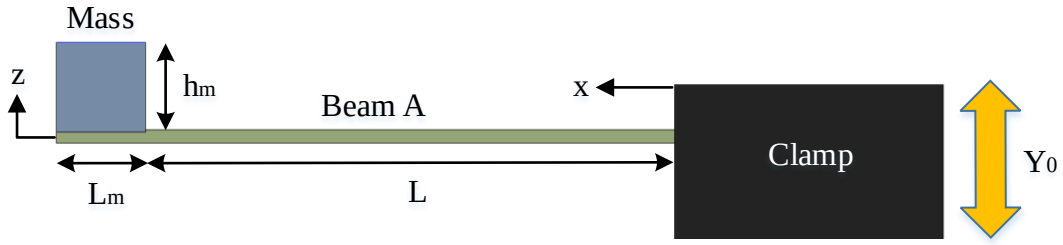

Figure 3. Schematic of a cantilever beam with a lumped mass placed on top of the free-end beam.

The transverse motion of the clamp-free cantilever beam subjected to a harmonic-base excitation at position x and time t can be described by the following equation.

$$z_{abs}(x,t) = z_{rel}(x,t) + Y_0 e^{i\omega t} \tag{1}$$

where $z_{\mathrm{abs}}(x,t)$ is the absolute vertical displacement of the vibrating beam, $z_{\mathrm{rel}}(x,t)$ is the vertical displacement of the beam relative to its clamped base and $Y_0(t)$ is the vertical amplitude of the base excitation. For simplicity, the base excitation is assumed to be in harmonic motion. Based on the Euler–Bernoulli beam theory, the equation of motion for undamped-free vibrations is given as:

$$EI\frac{d^4 z_{rel}(x,t)}{dx^4} + \rho A\frac{d^2 z_{rel}(x,t)}{dt^2} = 0 \tag{2}$$

where E is the Young's modulus of the beam, I is the second moment of area, ρ is the beam's density and A is the cross sectional area. Using the method of separation of variables, the term $z_{rel}(x,t)$ can be separated into its spatial and temporal components.

$$z_{rel}(x,t) = \sum_{n=1}^{\infty} \varphi_n(x)\eta_n(t) \tag{3}$$

where $\varphi_n(x)$ is the cantilever beam's modal-shape eigenfunction and $\eta_n(t)$ is the regular-response function. The homogeneous solution for $\varphi_n(x)$ is given by

$$\varphi_n(x) = D_1 cosh\frac{\beta_n}{L}x + D_2 sinh\frac{\beta_n}{L}x + D_3 cos\frac{\beta_n}{L}x + D_4 sin\frac{\beta_n}{L}x \tag{4}$$

where D_1, D_2, D_3 and D_4 are unknown constants, β_n is the modal frequency constant and L is the inner length of the beam as shown in Figure 2. By considering the static moment and the inertial contributions of the lumped mass at $x = L$, the following four boundary conditions can be derived [21].

$$EI\varphi_n(0) = EI\frac{d\varphi_n}{dx}(0) = 0 \tag{5}$$

$$EI\frac{d^2\varphi_n}{dx^2}(L) = {\omega_n}^2\left[I_t\frac{d\varphi_n}{dx}(L) + M_S\varphi_n(L)\right] \tag{6}$$

$$EI\frac{d^3\varphi_n}{dx^3}(L) = -{\omega_n}^2\left[m_t\varphi_n(L) + M_S\frac{d\varphi_n}{dx}(L)\right] \tag{7}$$

where ω_n is the modal natural frequency of the beam, I_t is the mass inertial contributions of the lumped mass, M_S is the static moment exerted by the lumped mass on the beam at $x = L$ and m_t is the total mass of the lumped mass and the overhang portion of the beam measured from $x = L$ to $x = L + L_m$. If a cuboid shape lumped mass was presumed, the terms m_t, I_t and M_S can be defined as

$$m_t = \rho h L_m w + \rho_m h_m L_m w_m \tag{8}$$

$$I_t = \rho_m h_m L_m w_m\left[\frac{1}{12}\left({L_m}^2 + {h_m}^2\right) + \frac{{L_m}^2}{4}\right] + \rho h L_m w\left[\frac{1}{12}\left({L_m}^2 + h^2\right) + \frac{{L_m}^2}{4}\right] \tag{9}$$

$$M_S = m_t\frac{L_m}{2} \tag{10}$$

where h and w are the thickness and width of the cantilever beam whereas ρ_m, h_m, L_m and w_m are the density, thickness, length and width of the lumped mass. It is important to note that equations (8), (9) and (10) are only valid for cuboid geometries and may need to be change if considering other geometries. Substituting the boundary conditions into equation (4) results in the following matrix.

$$\begin{bmatrix} O_{11} & O_{12} \\ O_{21} & O_{22} \end{bmatrix}\begin{bmatrix} D_1 \\ D_2 \end{bmatrix} = \begin{bmatrix} 0 \\ 0 \end{bmatrix} \tag{11}$$

where O_{11}, O_{12}, O_{21} and O_{22} are representations of the four boundary conditions. By equating the determinant of equation (11) to zero, the modal frequency constant, β_n, can be determined. The natural frequency of the beam can then be calculated using equation (12).

$$\omega_n = {\beta_n}^2\sqrt{\frac{Eh^2}{12\rho L^4}} \tag{12}$$

Therefore, the eigenfunction of the beam for the n^{th} mode shape is

$$\varphi_n(x) = D_2\left[cosh\frac{\beta_n}{L}x - cos\frac{\beta_n}{L}x - \frac{O_{21}}{O_{22}}\left(sinh\frac{\beta_n}{L}x - sin\frac{\beta_n}{L}x\right)\right] \tag{13}$$

Kim et al. [21] and Du Toit [22] solved for variable D_2 by normalizing equation (13) with the value of 2. However, the method presented by Erturk and Inman [23] to solve for the constant D_2 results in a more simple model. Here, the orthogonality conditions must be considered.

$$\frac{m_b}{L}\int_0^L[\varphi_n(x)]^2dx + \varphi_n(L)\left[m_t\varphi_n(L) + M_S\frac{d\varphi_n}{dx}(L)\right] + \frac{d\varphi_n}{dx}(L)\left[I_t\frac{d\varphi_n}{dx}(L) + M_S\varphi_n(L)\right] = 1 \tag{14}$$

$$L\int_0^L[\varphi_n(x)]^2dx - \varphi_n(L)EI\frac{d^3\varphi_n}{dx^3}(L) + \frac{d\varphi_n}{dx}(L)EI\frac{d^2\varphi_n}{dx^2}(L) = {\omega_n}^2 \tag{15}$$

By solving equations (14) or (15), the value of D_2 can be determined. For a steady state solution, a simple single-degree-of-freedom (SDOF) model can be used to represent the temporal term $\eta_n(t)$.

$$\ddot{\eta_n}(t) + 2\zeta_n\omega_n\dot{\eta_n}(t) + {\omega_n}^2\eta_n(t) = -\omega^2 Y_0 e^{i\omega t} F_n \tag{16}$$

where ζ_n is the mechanical modal damping ratio of the cantilever beam and F_n is the forcing function acting on the beam described by

$$F_n = \frac{m_b}{L}\int_0^L \varphi_n(x)dx + m_t\varphi_n(L) + M_S\frac{d\varphi_n}{dx}(L) \tag{17}$$

Equation (16) can easily be solved with reference to the solution for the general SDOF vibration model. The solution for equation (16) is

$$\eta_n(t) = \frac{Y_0 e^{i\omega t} F_n}{{\omega_n}^2 - \omega^2 + i2\zeta_n\omega_n\omega} \tag{18}$$

Substituting equations (18) and (13) into equation (3) results in the governing equation describing the relative vertical displacement of the vibrating beam,

$$z_{rel}(x,t) = \sum_{n=1}^{\infty} \frac{Y_0 e^{i\omega t} F_n}{{\omega_n}^2 - \omega^2 + i2\zeta_n\omega_n\omega}\varphi_n(x) \tag{19}$$

Considering only the first mode parameters ($n = 1$) and resonance ($\omega = \omega_1$), the maximum relative amplitude of the beam at $x = L$ can be evaluated as

$$z_{rel}(L)_{max} = \frac{Y_0\varphi_1(L)}{2\zeta_1}F_1 \tag{20}$$

To evaluate the amplitude of the beam at any point after $x = L$, it is sufficient to assume that the deflection curve of the beam behaves linearly after $x = L$ with the gradient of $\frac{d\varphi_1}{dx}(L)$.

$$z_{rel}(x > L)_{max} = z_{rel}(L)_{max} + sin\left\{tan^{-1}\left[\frac{Y_0}{2\zeta_1}\frac{d\varphi_1}{dx}(L)F_1\right]\right\} \tag{21}$$

2.2 Equation of motion for beam B and beam C

Figure 4 below describes a representation of the anti-phase resonance design.

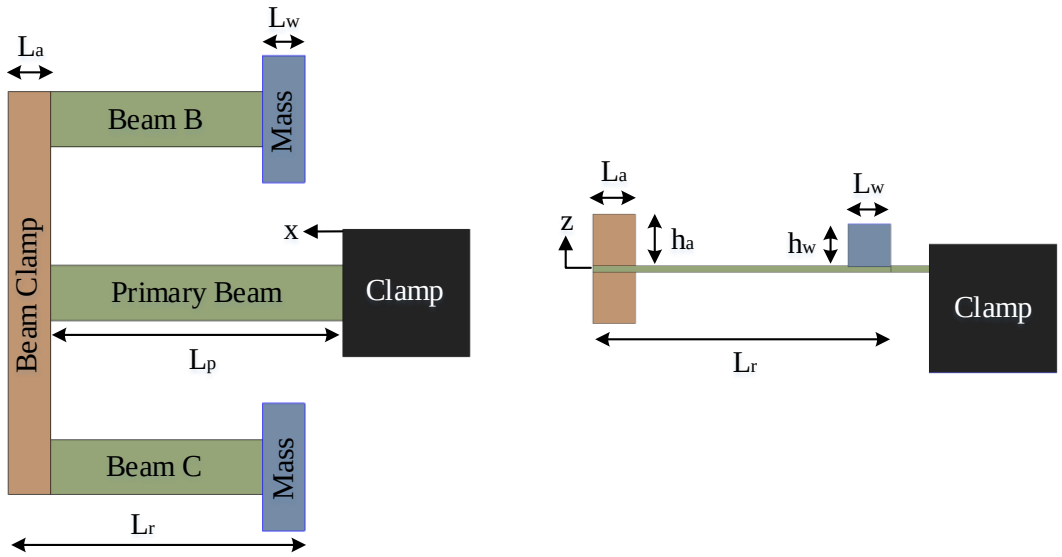

Figure 4. Schematic of the top view (left) and the side view (right) of the anti-phase resonance design.

To model the behaviour of beams B and C, the equation of motion for the primary beam must first be considered. Despite the complex design, the primary beam is still expected to display a linear behaviour at low amplitude vibrations due to its symmetrical properties in terms of geometry and weight. Therefore, the analytical equation presented for beam A would still be valid for the primary beam. However, the static moment and the inertial term of the lumped mass at $x = L_p$ becomes more complex due to its geometry. Assuming a cuboid shape for the cantilever beams, beam clamp and masses and applying the parallel axis theorem, the total lumped mass term (m_{tp}), the inertial

term (I_{tp}) and static moment (M_{sp}) term for the primary beam were derived as seen in equations (22), (23) and (24). Here, the mass and geometry of both beams B and C and the lumped mass placed on them are considered equal.

$$m_{tp} = m_a + m_o + 2(m_r + m_w) \tag{22}$$

$$I_{tp} = \frac{m_a}{12}\left({L_a}^2 + {h_a}^2\right) + \frac{1}{4}m_a{L_a}^2 + \frac{m_o}{12}\left({L_o}^2 + {h_o}^2\right) + \frac{1}{4}m_o{L_a}^2 + 2\left[\frac{m_r}{12}\left({L_r}^2 + {h_r}^2\right) + m_r\left(\frac{L_r}{2} - L_a\right)^2\right] + 2\left[\frac{m_w}{12}\left({L_w}^2 + {h_w}^2\right) + m_w\left(L_r - L_a - \frac{L_w}{2}\right)^2\right] \tag{23}$$

$$M_{sp} = m_{tp}\frac{L_a}{2} - 2\left[m_r\left(\frac{L_r - L_a}{2}\right) + m_w\left(L_r - L_a - \frac{L_w}{4}\right)\right] \tag{24}$$

where variable m, L, and h represents the mass, length and thickness of the object and subscripts a, o, r and w correspond to the beam clamp, primary beam overhang portion (measured from $x = L_p$ to $x = L_p + L_a$) , beam B/C and the lumped mass placed on beam B/C. Since the dynamic of beams B and C during vibration were not entirely considered in the governing equations, equations (22), (23) and (24) is only valid for first mode vibration. Assuming the vibrations in beams B and C to be much smaller than the primary beam, the modelling of beams B and C can be simplified to a linear motion with a gradient equal to $-\frac{d\varphi_1}{dx}(L)$. At resonance, the maximum relative amplitude of beams B and C can be determined by

$$z_{rel}(L_r)_{max} = z_{rel}\left(L_p\right)_{max} - (L_r - L_a)sin\left\{tan^{-1}\left[\frac{Y_0}{2\zeta_1}\frac{d\varphi_1}{dx}(L_p)F_1\right]\right\} \tag{25}$$

where $z_{rel}(L_r)_{max}$ is the maximum relative amplitude at the free-end tip of beam B or C and $z_{rel}\left(L_p\right)_{max}$ is the maximum relative amplitude of the primary beam at $x = L_p$. Equation (25) can easily be extrapolated for any desired position after L_r. It can be seen that if

$$(L_r - L_a)sin\left\{tan^{-1}\left[\frac{Y_0}{2\zeta_1}\frac{d\varphi_1}{dx}(L_p)F_1\right]\right\} \leq z_{rel}\left(L_p\right)_{max} \tag{26}$$

then the out-of-phase vibration cannot be achieved. Hence, the length of beams B and C must be properly selected to ensure that ensure that the deflection of beam B or C is greater than $z_{rel}\left(L_p\right)_{max}$.

2.3 Electromagnetic power output and phase shift equation

Faraday's law of electromagnetism and Kirchhoff's voltage law states that the voltage across a load resistance in a series type electromagnetic circuit is

$$V_L = NBL_c v_c \frac{R_L}{(R_c + R_L)}C_f \tag{27}$$

where V_L is the generated load voltage, N is the number of turns of coil, B is the strength of the magnetic flux, L_c is the effective length of the coil, v_c is the speed of the coil cutting through the magnetic flux, R_c is the resistance of the coil, R_L is the load resistance and C_f is the coil fill factor defined as

$$C_f = \frac{V_c}{V_w} \tag{28}$$

where V_c is the volume of the coil wire and V_w is the volume space of the total coil winding. Base on Ohm's law, the root-mean-square (RMS) power generated is

$$P = \frac{1}{\sqrt{2}(R_c + R_L)}\left[NBL_c v_c \frac{R_L}{(R_c + R_L)}C_f\right]^2 \tag{29}$$

It is important to now consider the effects of electromagnetic damping in addition to mechanical damping due to the presence of electromagnetic components. The maximum velocities of beam A at $x = L$ and beam B/C at free-end L_r during resonance is defined as

$$v_{max}^{a} = \frac{\omega_1^a Y_0}{2(\zeta_1^a + \zeta_e)}\varphi_1(L)F_1 \tag{30}$$

$$v_{max}^{bc} = \frac{\omega_1^{bc} Y_0}{2(\zeta_1^{bc} + \zeta_e)}\varphi_1(L_p)F_1 - \omega_1^{bc}(L_r - L_a)sin\left\{tan^{-1}\left[\frac{Y_0}{2(\zeta_1^{bc} + \zeta_e)}\frac{d\varphi_1}{dx}(L_p)F_1\right]\right\} \tag{31}$$

where v_{max}^{a} and v_{max}^{bc} are the maximum resonant velocities of beam A and beam B/C, ω_1^a and ω_1^{bc} are their respective first mode resonant frequency, ζ_1^a and ζ_1^{bc} is the first mode mechanical damping ratio of beam A and beam B/C and ζ_e is the electromagnetic damping contribution defined as

$$\zeta_e = \frac{(NBL_c C_f)^2}{2m_e\omega_1(R_c+R_L)} \tag{32}$$

where m_e is the effective mass of the beam and its lumped mass. It is easy to notice that the velocity term is actually the product of the beam's relative amplitude and its natural frequency. Hence, the same extrapolation method as equations (21) and (25) can be applied to obtain the velocity of beams A and B/C after the inner length. Since both the coil and the magnet in the anti-phase resonance design vibrates, the speed of the coil cutting through the magnetic flux would be equal to the relative velocity between these components. Assuming that the velocities of the coil and magnets are equal to v_{max}^{a} and v_{max}^{bc}, the governing equation describing the maximum RMS power output is

$$P_{max} = \frac{1}{\sqrt{2}(R_c+R_L)}\left[(NBL_c v_r)^2 \frac{R_L}{(R_c+R_L)} C_f\right]^2 \tag{33}$$

where P_{max} is the maximum RMS power output and v_r is the relative velocity between the coil and the magnets.

$$v_r = v_{max}^{a} - v_{max}^{bc} \tag{34}$$

Equation (33) shows that the maximum power output of the anti-phase resonance design is highly dependent on the relative velocity between beams A and B/C. To maximise the relative velocity between beams A and B/C, the phase difference between these two beams must be 180° so that when v_{max}^{a} is positive, v_{max}^{bc} will be negative. Naturally, the anti-phase resonance design should achieve 180° phase difference since beam A and beam B/C vibrate in the opposite directions. However, as the beams approach their respective natural frequencies, a shift in their phase will occur [24]. The first modal phase shift for beams A and B/C can be described by equations (35) and (36)

$$\theta_a = tan^{-1}\left(\frac{2\omega\omega_1^a\zeta_1^a}{\omega_1^{a^2}-\omega^2}\right) \tag{35}$$

$$\theta_{bc} = tan^{-1}\left(\frac{2\omega\omega_1^{bc}\zeta_1^{bc}}{\omega_1^{bc^2}-\omega^2}\right) - 180 \tag{36}$$

where θ is the phase angle in degrees of the beams with respect to the vibrating base and ω is the driving frequency of the vibrating base.

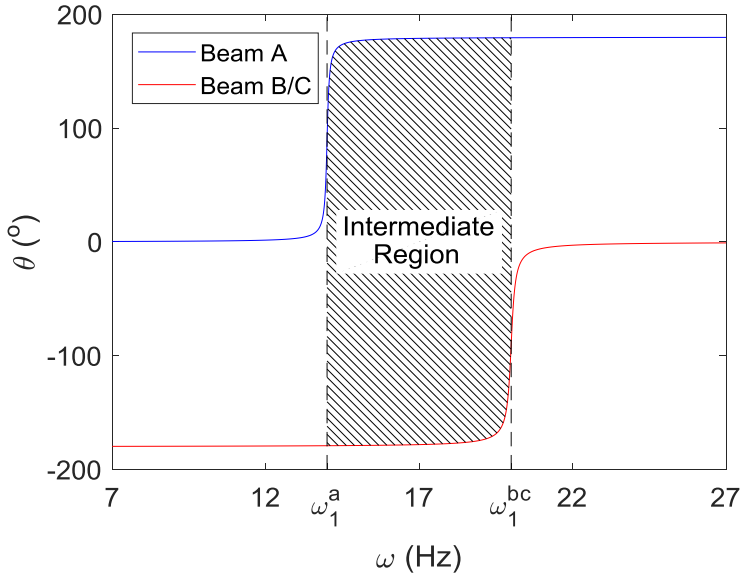

Figure 5. Phase shift in beams A and B/C for ω_1^a = 14Hz, ω_1^{bc} = 20Hz, ζ_1^a = 0.004 and ζ_1^{bc} = 0.005.

Equation (35) describes the phase angle of beam A to be approximately zero degrees before resonance, 90° at resonance and 180° after resonance. For beam B/C, the phase shift is -180° before resonance, -90° at resonance and

zero degrees after resonance. This is further illustrated in Figure 5. The region between the natural frequencies of beams A and B/C in known as the intermediate region. The difference between equations (35) and (36) represents the phase difference between beams A and B. Equations (35) and (36) also states that the ideal condition to maintain a 180° phase difference between beam A and beam B/C at resonance, the natural frequencies and damping ratios of both beams must be equal.

3. Experiment setup

In this work, an experiment was conducted to determine the power output generated by the anti-phase resonance design and compare it with the power output of beam A, which represents a conventional cantilever-based electromagnetic harvester design. Tables 1 and 2 describe the properties and dimensions of the cantilever beams used in the experiment and their respective lump masses. To simplify analytical calculations later, all masses added to the beams will resume an equivalent cuboid shape. All cantilever beams were made of the same glass fiber material. The damping ratios of beam A and the primary beam were pre-determined from their frequency response curves using the half-power bandwidth method [25].

Table 1. Specifications of all the cantilever beams used in the experiment.

Beam	Beam A	Primary Beam	Beam B/C
E (GPa)	25	25	25
ρ (kgm^{-3})	1850	1850	1850
L_t(mm)	70	80	70
t (mm)	1.5	1.5	1.5
w (mm)	13	13	13
ζ_1	0.0039	0.0045	-

Table 2. Specifications of the lumped masses used in the experiment.

Type of mass	Pair of magnets	Beam clamp	Coil
Location	Beam A	Primary Beam	Beam B
m_t (g)	47.0	45.9	8.3
L (mm)	25	10	10
t (mm)	12	24	12
w (mm)	30	98	30

Figure 6 describes the actual experiment setup and the schematic of the experiment setup. Additional mass was added to beam C until the measured amplitude and phase at the clamped end of beams B and C are equal. This means that the design has achieved symmetrical balance. Note that the equivalent cuboid shape of the coil in Table 2 is taken from the same geometry as the added mass on beam C as seen in Figure 6. Two laser displacement sensors were used to measure the output response of beam A and B at their respective free-ends. The coil was connected to a load resistor before being connected to a data acquisition device (DAQ). The output of both laser displacement sensors were amplified and sent to the DAQ. The DAQ device then sends the voltage readings from the coil and the displacement readings from the laser displacement sensors to a computer for analysis. The DAQ device was controlled using LabVIEW whereas all post-experiment analysis were conducted using MATLAB.

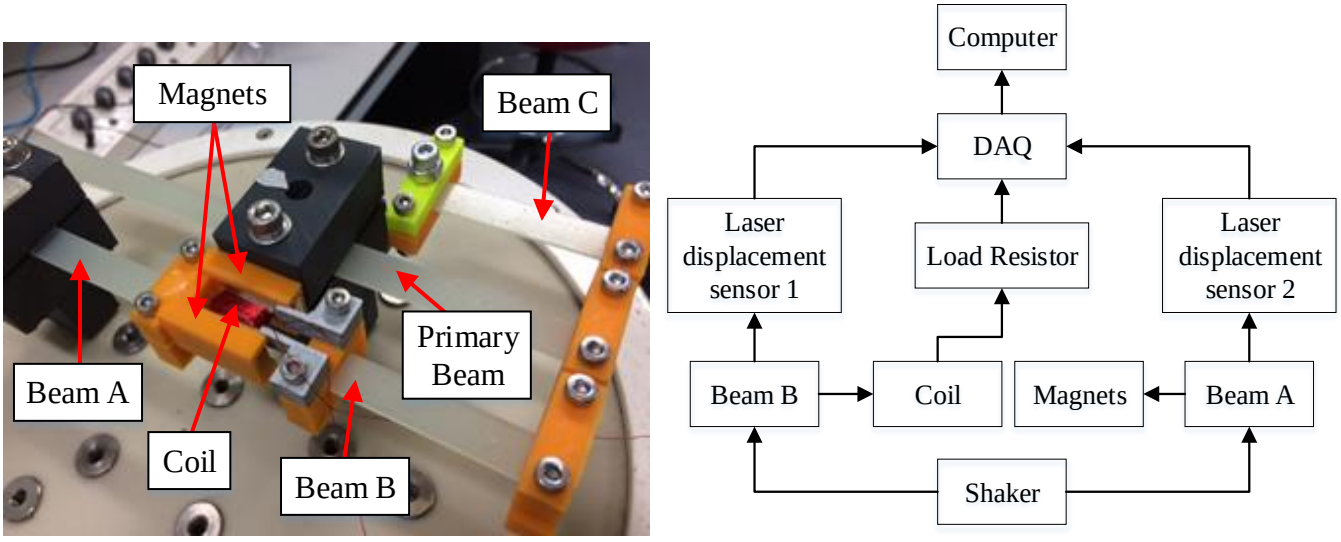

Figure 6. Diagram of the actual experiment setup (left) and a schematic representation of the experiment setup (right).

The properties of the coil and the magnets used are listed in Table 3. A base acceleration magnitude of 0.1 g was used for all conducted experiments, where 1 g is equal to an acceleration of 9.81 ms^{-2}.

Table 3. Specifications of the coil and magnets used in the experiment.

Coil		Magnets	
L_c (mm)	38	Type	Neodymium N35
N	100	Number of magnets	2
R_c (Ω)	2.5	B (T)	0.195

4. Results and analysis

An experiment was conducted to determine the power output of the anti-phase resonance design under ideal condition, where the natural frequency and damping ratio of beams A and B are equal. Additional mass was slowly added onto beam A until the natural frequencies of beams A and B were equal, resulting in the lumped mass value shown in Table 1. This brought about a natural frequency of 17.24 Hz for both beams as seen in Figure 7.

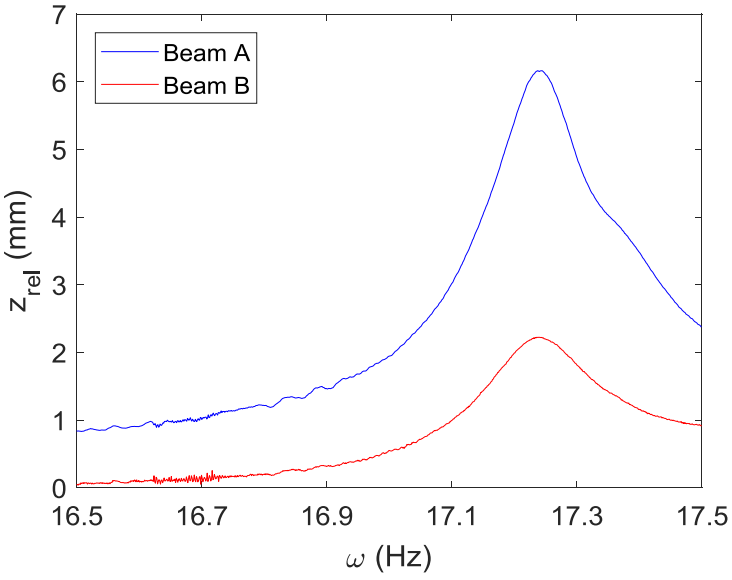

Figure 7. Frequency response plots of beams A and B under the ideal condition.

The damping ratios of the beams were not optimized due to the difficulty of simultaneously maintaining equal natural frequency while adjusting the damping ratio of both beams. Nevertheless, the damping ratio of both beams only differ by 15%. Figure 8 shows the actual and the schematic of the coil winding used in the experiment.

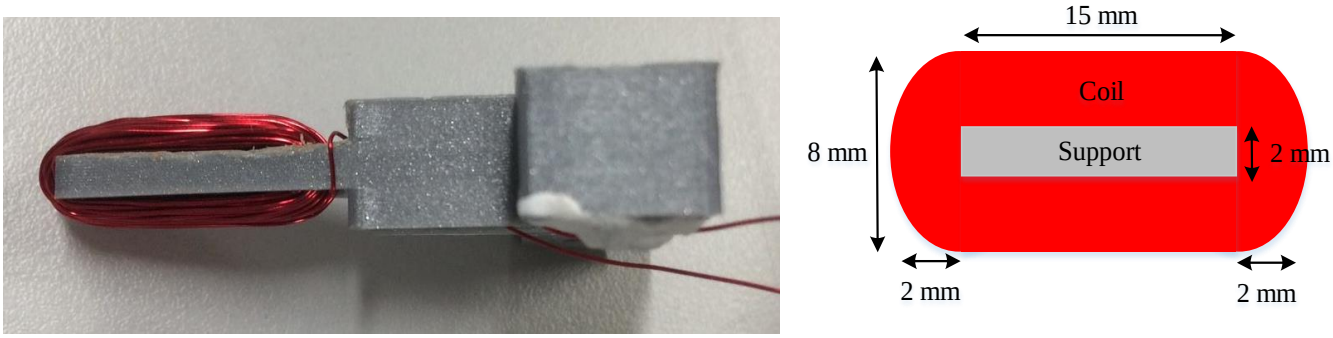

Figure 8. Actual diagram of coil (left) and specifications of coil measurements (right).

The widths of the coil winding and the support are 7 mm and 6 mm respectively. The total length of the coil used is 5.1 m, with an extra 2.1 m overhang. This gives a total winding coil volume of V_c = 250 mm^3 and a total occupied volume space of V_w = 836 mm^3. Hence, from equation (27), this leads to a coil fill factor of C_f = 0.30.

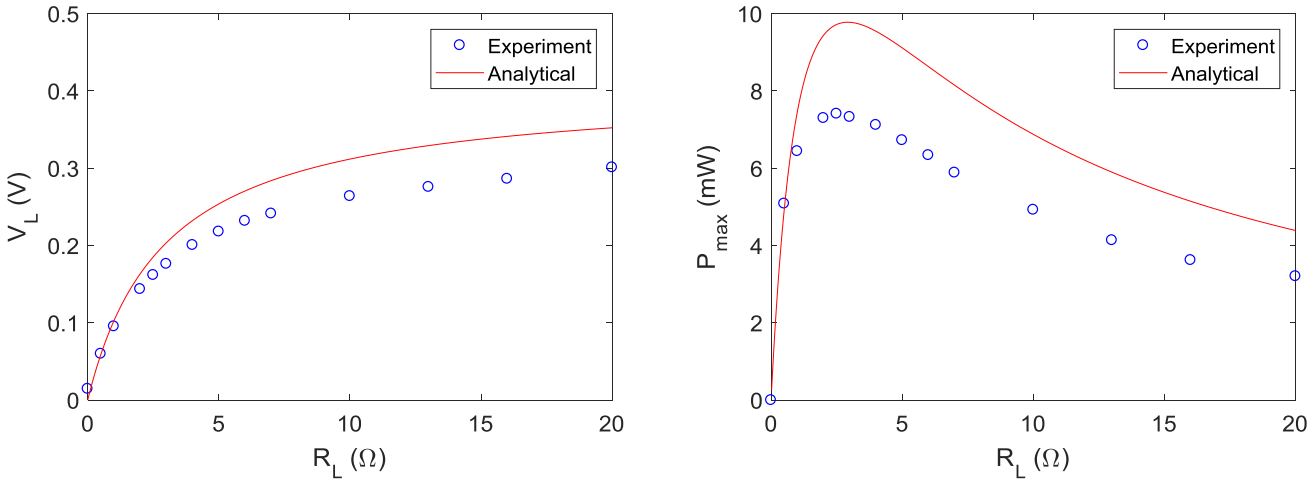

Figure 9. Results of load voltage (left) and maximum power output (right) under different load resistance input.

Yang et al. [26] showed that for every coil resistance, there exists an optimum load resistance value where maximum power would be produced. Hence, the anti-phase resonance design was tested under different load resistances to determine this optimum value. The resulting load voltage and the maximum RMS power output obtained were plotted against its corresponding load resistance as shown in Figure 9. Figure 9 shows that both the analytical and experiment results defined the optimum load resistance value as 2.5 Ω. Saha et al. [27] reported that when the electromagnetic damping is much less than the mechanical damping, the optimum load resistance is equal to the coil resistance. Figure 10 illustrates the plot of electromagnetic and mechanical damping of beam A and beam B. The maximum recorded electromagnetic damping ratio for beams A and B was 0.0016 and 0.00097 correspondingly, which is less than their respective mechanical damping ratios. Hence, the results presented here are in agreement with the previous work. The maximum power output of the anti-phase resonance design under a load resistance of 2.5 Ω was recorded. It can be seen that there is an approximate 25% difference between the analytical and experimental results, which can be attributed to the effect of counter-electromotive forces that opposes the current flow in the coil, hence reducing the voltage. Nevertheless, a good correlation between the experimental and analytical results can be observed in Figures 9 and 10, therefore verifying the validity of the derived governing equations.

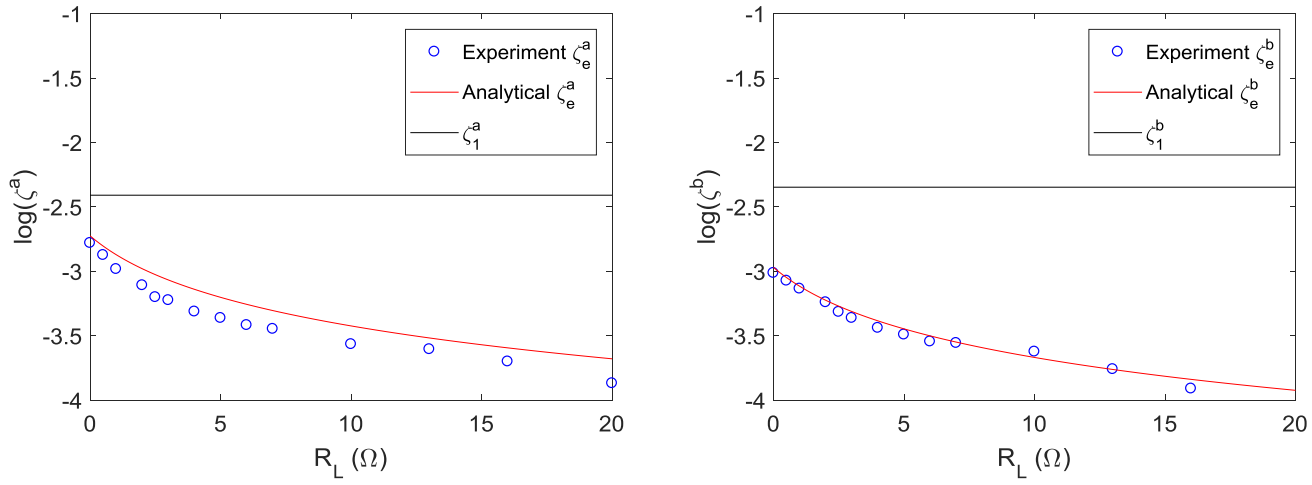

Figure 10. Results of electromagnetic damping ratios under different load resistance input for beam A (left) and beam B (right).

4.1 Power output and power density comparison.

Figure 11 describes the variation in maximum velocities for beams A and B under different load resistance. In the experiment, the velocities of beams A and B were recorded at their free-ends. Hence, an extrapolation was made using the same method as equations (21) and (25) to account for the velocity at the center of the coil and the permanent magnets.

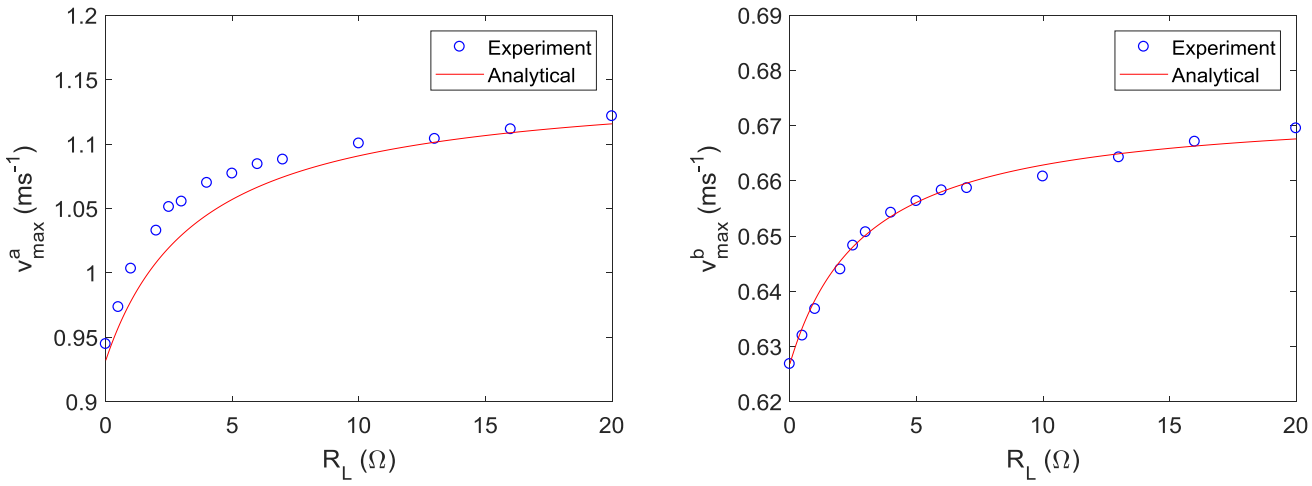

Figure 11. Results of extrapolated maximum velocities under different load resistance input for beam A (left) and beam B (right).

The velocities of beam A observed to be much higher than the velocities of beam B. Therefore, only the individual power output of beam A will be compared with the anti-phase resonance design as the power output of beam A will undeniably be larger than beam B. A good correlation was observed between the analytical equations and experimental results in Figure 11. The experiment was then conducted to determine the maximum individual power output of beam A which represents a conventional design. This was performed by fixing the same coil that was attached to beam B onto the shaker using a clamp. The same load resistance of 2.5 Ω was used to maximise the power output. Figure 12 shows the comparison between the voltage and power output of the anti-phase resonance design and the conventional design.

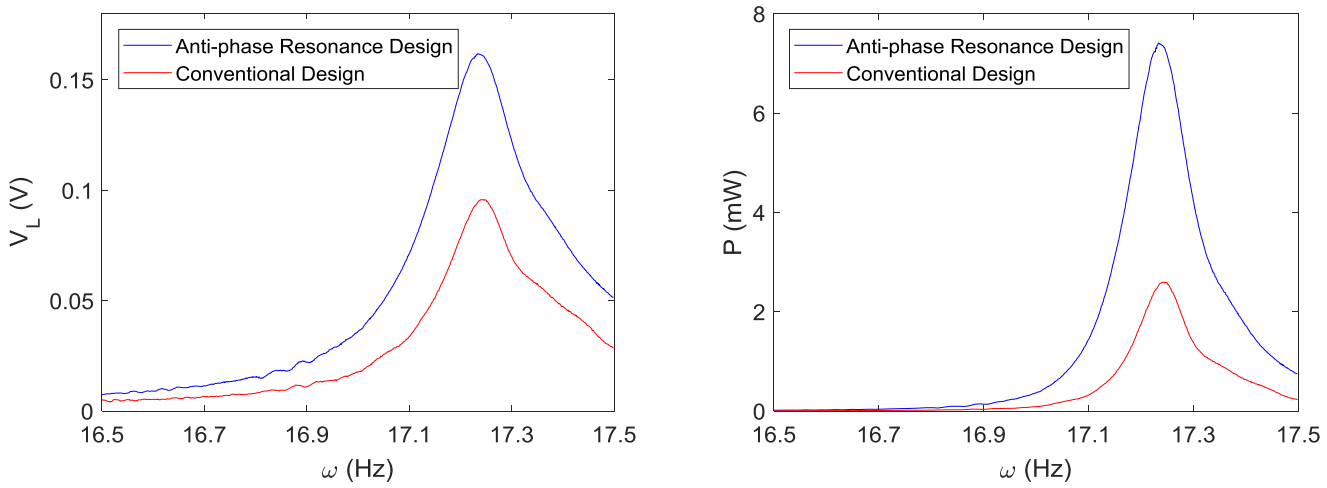

Figure 12. Comparison of the load voltage (left) and power output (right) between two designs.

Results in Figure 12 shows that the anti-phase resonance design is superior in terms of both power and bandwidth as compared to the conventional design. The anti-phase resonance design recorded a 69% increase in maximum load voltage and a power output of 7.4 mW at resonance resulting in a 185% increase in the maximum power when compared with the conventional design. Although the individual power output of beam B was not recorded, it is expected to be lower than that for beam A as discussed earlier. Therefore, it can be concluded that the power output of the anti-phase resonance design is higher than the sum of the individual power outputs from beams A and B. The reason for this is because individually, beams A and B vibrate at a relative velocity of $v_r = v_{max}^a$ and $v_r = v_{max}^b$ respectively. Therefore, the anti-phase resonance design would have a relative velocity of $v_r = v_{max}^a + v_{max}^b$. Since P_{max} is proportional to ${v_r}^2$, the maximum power output of the proposed method would always be higher than the sum of the individual power output from the two beams, because $\left(v_{max}^a + v_{max}^b\right)^2$ is always higher than ${v_{max}^a}^2 + {v_{max}^b}^2$ for any positive input value. Hence this explains why the power output of the anti-phase resonance design is higher than the sum of individual power outputs from beams A and B. The anti-phase resonance design also recorded an operational bandwidth of 0.095 Hz, which is 22% higher than the operational bandwidth of 0.078 Hz obtained from the conventional design. In addition, the load voltage and the power output of the anti-phase resonance design is observed to be consistently higher than the conventional design for the range of 1 Hz. This shows that the anti-phase resonance design is capable of providing an improved output at non-resonant frequencies.

Normally, the performance of an electromagnetic vibration energy harvester is evaluated from their power densities, which is generally the ratio of the maximum output power to the practical volume of the harvester. The practical volume for large harvesters is defined as the estimated volume of the beam, magnets, coils and space swept by the vibrating beam [28]. For simplicity, the following cuboid areas in Figure 13 are assumed as their estimated practical areas. The practical height is assumed the same for both designs with a height of 35 mm. This assumption is valid since the highest peak recorded from the experiment was located at beam A.

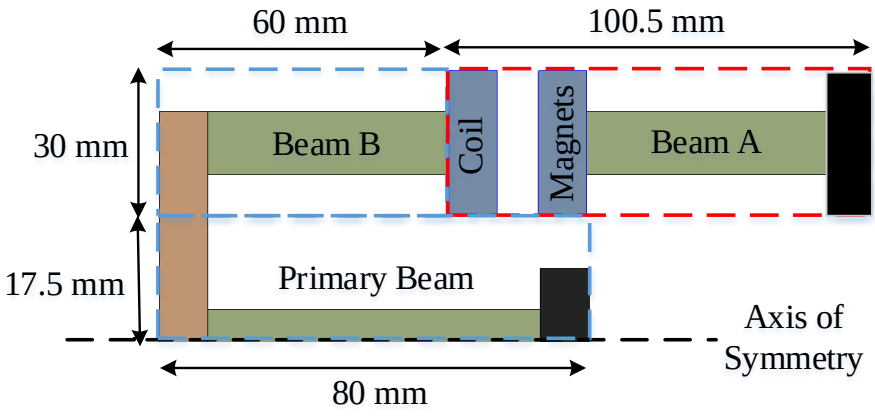

Figure 13. Schematic representing the practical volume of the anti-phase resonance design and the conventional design.

Only half of the volume of the anti-phase resonance design was considered in relation with the experiment. The area covered by the red dashed box marks the practical volume of the conventional design whereas the total area covered by the blue and red dashed boxes represents the practical volume of the anti-phase resonance design. The maximum recorded power output and the total practical volume of both designs are tabulated in Table 4.

Table 4. Maximum power output and total practical beam volume of the anti-phase resonance design and the conventional design.

Design	Anti-Phase Resonance Design	Conventional Design
P_{max} (mW)	7.4	2.6
Total practical volume (mm^3)	217525	105525

The power density in terms of beam volume for the anti-phase resonance design and the conventional design are 34.0W/m^3 and 24.6 W/m^3 respectively. This shows a 38% increase in power density for the anti-phase resonance design. It is clear that if the volume of the clamps, magnets and coil were kept constant in the design, the power density of the design would be highly dependent on the beam volume. Hence, the velocity ratio of v^a_{max}/v^b_{max} would play a crucial role in determining the performance of the anti-phase resonance design. Figure 14 describes the plot of normalised power density, PD_N, against the ratio of v^a_{max}/v^b_{max} for different beam volume ratios of the anti-phase resonance design beam volume to conventional design beam volume, Vol_r. The conventional design in Figure 14 refers to the individual power output of beam A.

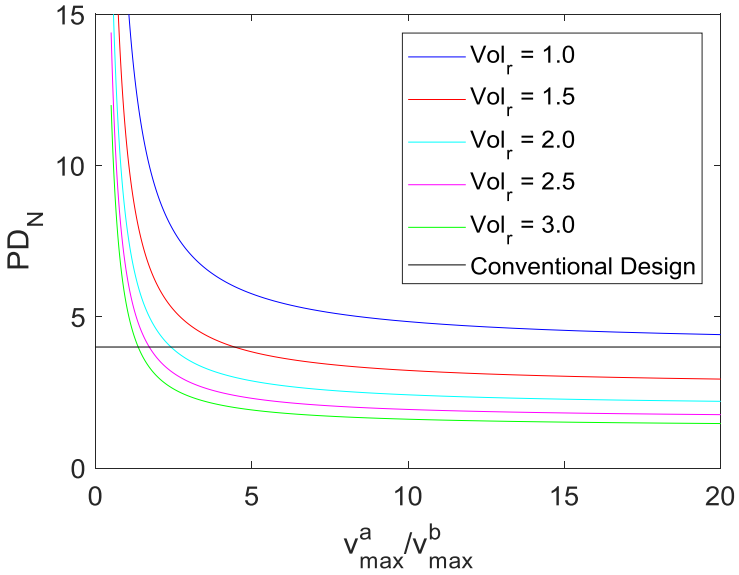

Figure 14. Variation in normalised power densities under different velocity ratios for five different beam volume ratios.

The analysis in Figure 14 states that if the total beam volume of the anti-phase resonance design is equal to the conventional design, then the anti-phase resonance design will always produce a higher power density than the conventional design for any v^a_{max}/v^b_{max} values. However, as Vol_r increases, the ratio of v^a_{max}/v^b_{max} for the anti-phase resonance design to have a higher power density than the conventional design reduces. For example, if $Vol_r = 2.5$, then the maximum ratio of v^a_{max}/v^b_{max} the anti-phase resonance design can have for it to be better than the conventional design in terms of power density is 1.7. Any higher will compromise the power density of the design.

4.2 Phase analysis of the anti-phase resonance design.

Figure 15 describes the time-displacement curves of beams A and B at resonance for the experiment performed.

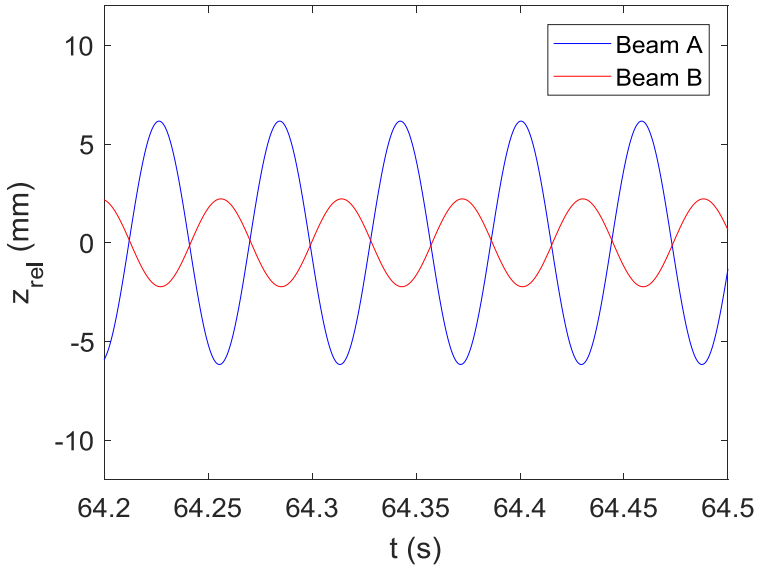

Figure 15. Amplitude-time plots of beams A and B at resonance recorded from experiment.

The phase difference between the two beams was calculated using the following formulae.

$$\Delta\theta = \frac{1}{2\pi} 360 \Delta t \omega_n \tag{37}$$

where $\Delta\theta$ is the phase difference in degrees and Δt is the time lag between the time-displacement curves of beams A and B. The phase difference in Figure 14 was determined to be 175°. This value is slightly lower than the ideal phase difference of 180° which may be due to the difference in damping ratios between the two beams.

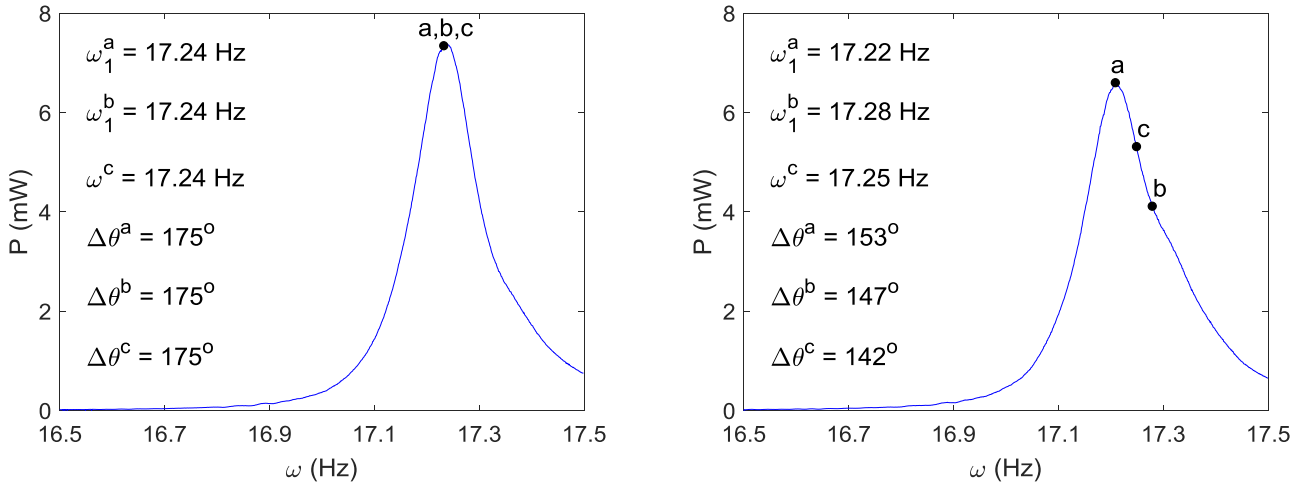

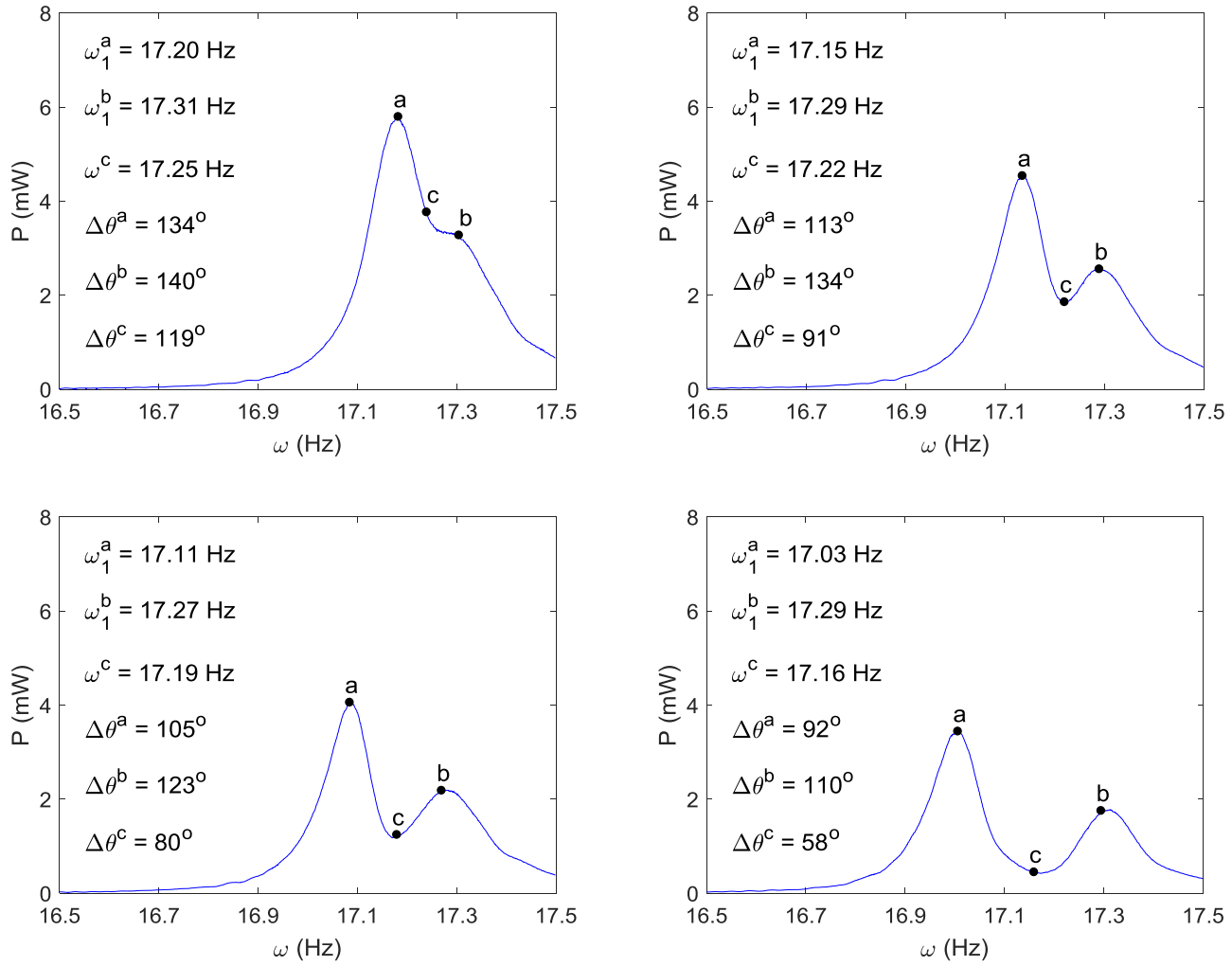

Figure 16. Variation in power output of the anti-phase resonance design under different natural frequencies of beams A and B.

The experiment results in Figure 15 was performed under the ideal condition of matched frequencies. The experiment was then continued to explore the effect of the phase difference on the power output of the anti-phase resonance design. This was done by adding a mass to the beam A so that the natural frequency and hence the phase difference between beams A and B was increased. The load resistance of 2.5 Ω was maintained in the experiment. Since the natural frequencies of beams A and B are now different, the phase difference was recorded at three regions, namely regions a, b and c. Regions a and b correspond to the two natural frequencies of beams A and B whereas region c is the centre of the intermediate region between the two natural frequencies as described by Figure 5. Figure 16 describes the power curves for six different experiments. The phase differences and frequencies of regions a, b and c are shown on each plot. The first resonance peak in the plots represents beam A whereas the other peak represents beam B. It can be observed that as the difference between the natural frequencies of beams A and B ($\Delta\omega_1$) increases, the phase differences in all recorded regions decreases as shown in Figure 16.

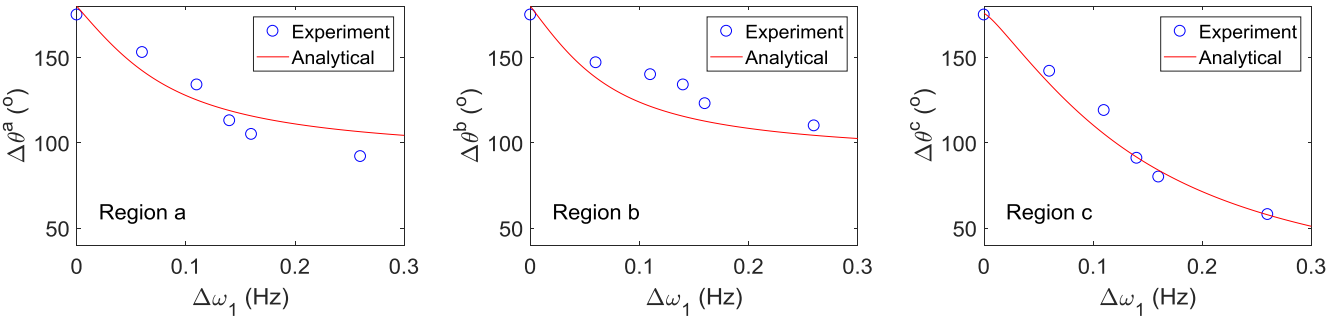

Figure 17. Variation in phase difference between beams A and B at regions a, b and c under different variations of natural frequency values. The analytical results were calculated using equations (35) and (36).

Figure 17 shows that the phase difference at both resonance peaks are almost similar. The phase difference recorded the lowest value at region c, signifying that this region experiences the largest decrease in phase difference as compared to other regions. In terms of power output, the power at each region is observed to decrease as the phase difference between the two beams decreases. This is because the relative velocity decreases in terms of phase and magnitude when the phase difference decreases, hence decreasing the power. Nevertheless, the operational bandwidth is seen to increase when the phase difference increases. Equations (35) and (36) states that when the phase difference between the two beams drops below 90°, the relative velocity would deteriorate and become lower than its individual velocity output. This is because below a phase difference of 90°, the velocity of beam B would have a positive magnitude when beam A reaches its peak positive velocity. Therefore, the last two plots in Figure 16 would experience a worse power output at region c if compared with the individual power outputs of beams A and B.

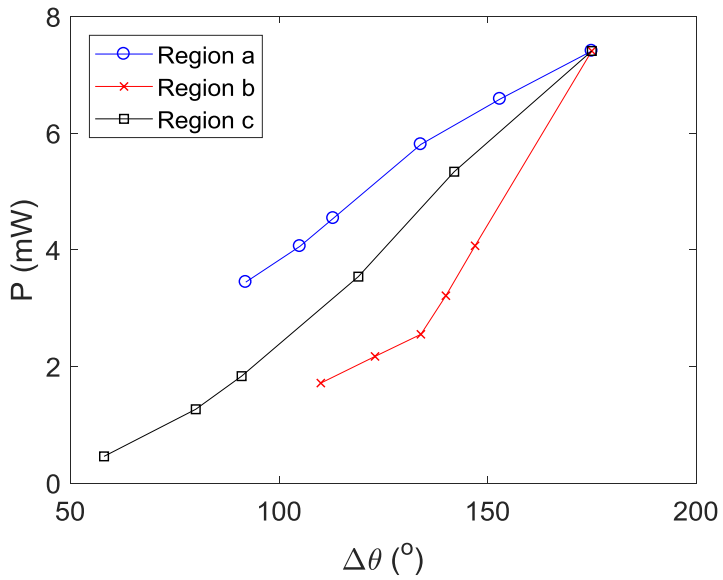

Figure 18. Variation in power outputs at regions a, b and c under different phase difference.

Figure 18 demonstrates the variation in power output with phase difference. A 94% decrease in power output was recorded at region c when the phase difference between beam A and B decreases 67% from 175° to 58°. For regions a and b, the power decreased by 53% and 77% for a decrease in phase difference of 47% and 37%. Although the decrease in phase difference is seemingly large, it only amounts to a mere 1.5% difference in the natural frequencies of beams A and B. Hence, this shows the importance of fine tuning the frequencies of both beam in order to achieve optimum power output. The reason that the experiment outcomes display a large change in phase difference for a small variance in natural frequencies of beams A and B may be due to the relatively low damping ratio of glass fiber material, resulting in a narrow bandwidth. It is believed that if a different material with larger damping capacity was used (e.g.: polymers), the anti-phase resonance design would be able to sustain a high phase difference value over a wider variation of natural frequencies, especially at region c. However, this will also compromise in terms of the power output. Overall, this analysis suggests that to maximize the performance of the

anti-phase resonance design, the frequencies of beams A and B must be equal. Even a 1.5% difference in frequency between the two beams can lead to a huge drop in phase difference and hence the power output.

The concept of anti-phase resonance generally applies the principle of superposition to achieve a significant increase in power. Wong et al. [29] showed that superposition in the resonance peak can also be achieved using a multi-degree-of-freedom topology. Their work reported similar results to Figure 16 in terms of amplitude and bandwidth. However, Wong et al.'s application of superposition was under the condition of the same phase motion. In this case, to amplify the power output, the amplitude or velocity of the vibrating system must be physically increased. On the other hand, using the concept of anti-phase motion can result in the same increase in power output under a much lower amplitude due to the theory of a relative motion, although it is well aware that this concept may only be beneficial for electromagnetic harvesters.

4.2 Gain analysis of an electromagnetic vibration energy harvester.

For a regular cantilever beam with a lumped mass, the gain of beam would decrease with the increase in the effective mass due to the increase in mechanical damping. However, for a cantilever beam-based electromagnetic vibration energy harvester, equation (32) describes the electromagnetic damping to be inversely proportional to effective mass of a cantilever beam and its lumped mass.

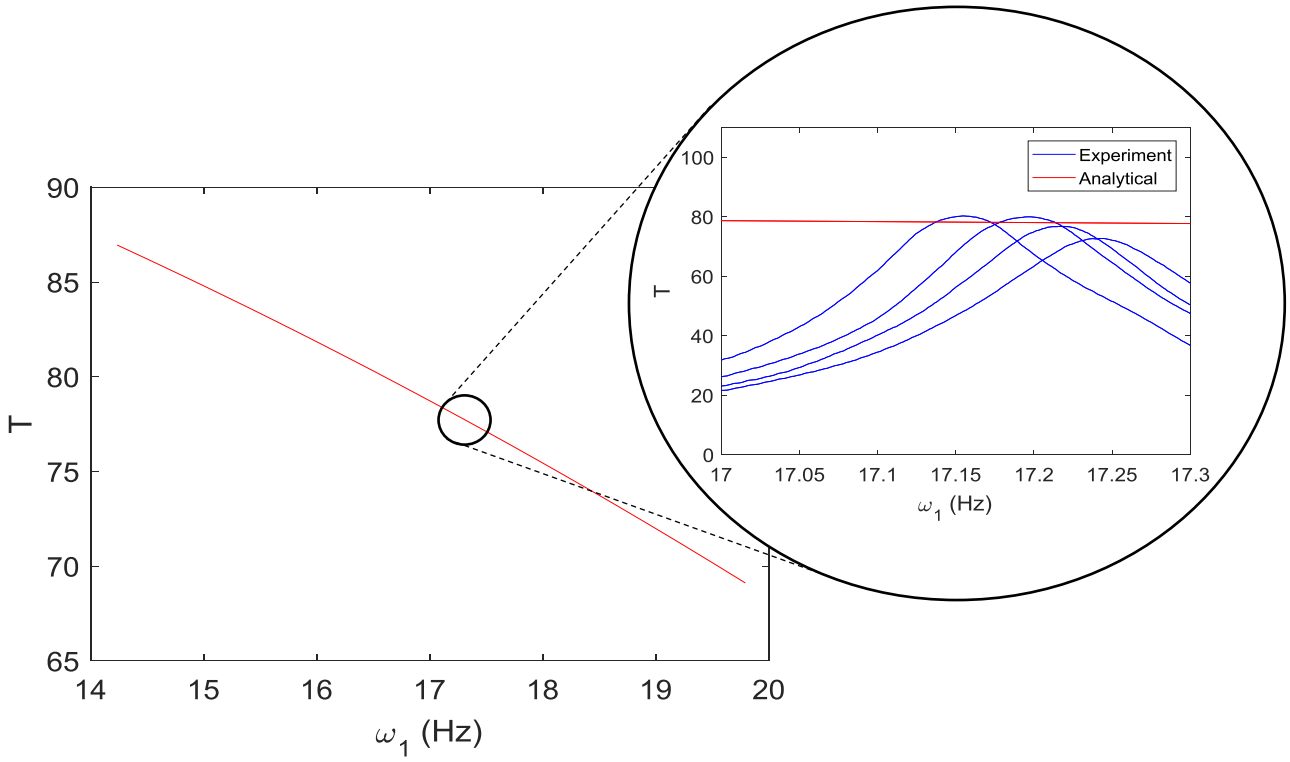

Figure 19. Variation in natural frequency and gain of beam A. The zoomed in section shows the comparison between experimental and analytical results.

Theoretically, increasing the effective mass of the system in this case would reduce the total damping and increase gain, hence increasing the power output of the harvester. Conversely, this theory is only true if the effective mass of the beam was increased by adding bulk masses on the beam. If instead magnets are added, the increase in magnet volume would increase the magnetic field strength, which may result in an increase of electromagnetic damping. The effect of increasing the effective mass is naturally reflected in the natural frequency of the beam-mass system. Figure 19 describes the analytical variation in output gain against the natural frequency for beam A, where the gain, T, is defined as the ratio of the relative amplitude, z_{rel} to the base excitation amplitude, Y_0.

The mechanical damping is assumed to be constant. The zoomed in section of Figure 19 shows the comparison between the analytical solution and the experimental gain results of beam A from the same experiment representing the first four plots of Figure 16. The analytical solution in Figure 19 demonstrated a 0.9% increase in gain per gram

of bulk mass added onto the beam whereas the experimental results recorded an average of 4.0% increase in gain per gram. Despite the discrepancies in the results, both results displayed an increasing trend in gain when the effective mass of the beam increases. This is due to the decrease in the electromagnetic damping ratio of the harvester. One may argue that increasing the effective mass would also lead to an increase in the mechanical damping ratio. However, the reduction in total damping shown by the experimental results in Figure 19 suggest that the decrease in the electromagnetic damping is larger than the increase in the mechanical damping for the glass fiber material. It is uncertain if other material would also lead to the same results as the glass fiber. Experimental verification for the analytical results in Figure 19 for a wider range of natural frequency reduction (by adding heavier bulk mass) was not explored in this study. Hence, the investigation on this matter would be considered in future works.

5. Conclusion

The paper presented a novel method to improve the power output of an electromagnetic vibration energy harvester through the concept of anti-phase resonance. This concept theorised that if the coil and the magnets of an electromagnetic vibration energy harvester can be made to vibrate out-of-phase from each other at resonance, the maximum power output generated would significantly increase due to an increase in the relative velocity of the coil cutting through the magnetic flux. A new harvester design was proposed to enable the coil and magnets to achieve anti-phase resonance under the same base excitation input. Under a base excitation acceleration of 0.1 g, the anti-phase resonance design displayed a 185% increase in power output and a 22% increase in operational bandwidth when compared with the individual output of a single beam design. In addition, the power output of the anti-phase resonance design was observed to be higher than the sum of power outputs from two individual beams vibrating with the same velocities. In terms of power density, the proposed method recorded a 38% higher power density than the conventional design. A phase analysis was performed to investigate the effect of phase difference on the power performance of the anti-phase resonance design. It was found that a 1.5% difference in natural frequencies between the coil and the magnets can result in a maximum of 47% decrease in phase difference at the resonant regions and a 67% decrease in phase difference at the intermediate region between the two resonant frequencies. This in turn led to a 53% decrease in maximum power at the resonant regions and a 94% decrease in power at the intermediate region. Therefore, this analysis defines the importance of fine-tuning the natural frequency of the coil and the magnets to be equal in order to achieve maximum power output. Finally, it was shown that by increasing the effective mass of a glass fiber cantilever beam, the total damping reduces leading to an increase in the overall gain of the harvester. Further works in this study would focus on the optimisation of the anti-phase resonance design to further maximise its power output. In addition, the effect of increasing the effective mass on the power output of a cantilever beam-based electromagnetic vibration energy harvester will be further explored in detail.

References

[1] Y. Ma, Q. Ji, S. Chen, G. Song, An experimental study of ultra-low power wireless sensor-based autonomous energy harvesting system, J. Renew. Sustain. Energy 9 (2017) 054702.

[2] B. Buchli, F. Sutton, J. Beutel, L. Thiele, Towards enabling uninterrupted long term operation of solar energy harvesting embedded systems. In: Wireless sensor networks. New York: Springer; 2014. pp. 66–83.

[3] S. Priya, Modeling of electric energy harvesting using piezoelectric windmill, Appl. Phys. Lett. 87 (18) (2005) 184101.

[4] Y. Shi, Y. Wang, Y. Deng, H. Gao, Z. Lin, W. Zhu, H. Ye, A novel self-powered wireless temperature sensor based on thermoelectric generators, Energy Convers. Manage. 80 (2014) 110–116.

[5] C.B. Williams, R.B. Yates, Analysis of a micro-electric generator for microsystems, Sens. Actuat. A. 52 (1996) 8–11.

[6] C.K. Thein, B.L. Ooi, J.S. Liu, J.M. Gilbert, Modelling and optimization of a bimorph piezoelectric cantilever beam in an energy harvesting application. J. Eng. Sci. Tech. 11(2) (2016) 212–227.

[7] K. Sang-Gook, S. Priya, I. Kanno, Piezoelectric MEMS for Energy Harvesting, MRS Bulletin 37.11. (2012) 1039–1050.

[8] S.P. Beeby, R.N Torah, M.J. Tudor, P. Glynne-Jones, T. O'Donnell, C.R. Saha, S. Roy, A micro electromagnetic generator for vibration energy harvesting, J. Micromech. Microeng. 17 (2007) 1257–1265.

[9] C.K. Thein, J.S. Liu, Numerical modeling of shape and topology optimisation of a piezoelectric cantilever beam in an energy‐harvesting sensor. Eng. Comp. 33 (2017) 137–148.

[10] Z. S. Chen, Y. M. Yang, G. Q. Deng, Analytical and Experimental Study on Vibration Energy Harvesting Behaviours of Piezoelectric Cantilevers with Different Geometries, Int. Conf. on Sustainable Power Generation and Supply (SUPERGEN), 2009, Nanjing, China.

[11] B.L Ooi, J.M Gilbert, Design of wideband vibration-based electromagnetic generator by means of dual-resonator, Sens. Actuat. A. 213 (2014) 9–18.
[12] F. Cottone, R. Frizzell, S. Goyal,G. Kelly, J. Punch, J. Intel. Mater. Syst. Struct. 25(4) (2014) 443–441.
[13] L. Deng, Z. Wen, X. Zhao, Theoretical and experimental studies on piezoelectric‐electromagnetic hybrid vibration energy harvester, Microsyst. Technol. 23 (2017) 935–943.
[14] H. Yu, J. Zhou, X. Yi, H. Wu, W. Wang, A hybrid micro vibration energy harvester with power management circuit, Microelectron. Eng. 131 (2015) 36–42.
[15] M.F. Abdul Rahman, S.L. Kok, N. Mat Ali, R.A. Hamzah, K.A. Abdul Aziz, Hybrid Vibration Energy Harvester Based On Piezoelectric and Electromagnetic Transduction Mechanism, IEEE Conf. on Clean Energy and Technology (CEAT), 2013, Langkawi, Malaysia.
[16] P. Kim, M.S. Nguyen, O. Kwon, Y.J. Kim, Y.J. Yoon, Phase-dependent dynamic potential of magnetically coupled two-degree-of-freedom bistable energy harvester, Scientific Reports 6 (2016) 34411.
[17] B. Andòa , S. Baglioa , L. Latorreb , F. Maiorcaa , P. Nouetb , C. Trigonaa, Magnetically-Coupled Cantilevers with Antiphase Bistable Behavior for Kinetic Energy Harvesting, Proc. Eng. 47 (2012) 1065–1068.
[18] D. Yurchenko, Z.H. Lai, G. Thomson, D.V. Val, R.V. Bobryk, Parametric study of a novel vibro-impact energy harvesting system with dielectric elastomer, App. Energy. 208 (2017) 456–470.
[19] D. Yurchenko, D.V. Val, Z.H. Lai, G. Gu, G. Thomson, Energy harvesting from a DE-based dynamic vibro-impact system, Smart Mater. Struct. 26 (2017) 105001.
[20] B.C. Lee, G.S. Chung, Design and analysis of a pendulum-based electromagnetic energy harvester using antiphase motion, IET Renew. Power Gener. 10 (2016) 1625–1630.
[21] M. Kim, M. Hoegen, J. Dugundji, B.L. Wardle, Modeling and experimental verification of proof mass effects on vibration energy harvester performance, Smart Mater. Struct. 19 (2010) 045023.
[22] N.E. Du Toit, Modeling and Design of a MEMS Piezoelectric Vibration Energy Harvester, Masters Thesis, 2005.
[23] A. Erturk, D.J. Inman, On mechanical modelling of cantilevered piezoelectric vibration energy harvesters', J. Intel. Mater. Syst. Struct. 19 (2007) 1311–1325.
[24] A. Badel, E. Lefeuvre, Wideband Piezoelectric Energy Harvester Tuned Through its Electronic Interface Circuit, J. Phys. Conf. Ser. 557 (2014) 012115.
[25] A. Cammarano, S.A. Neild, S.G. Burrow, D.J. Inman, The bandwidth of optimized nonlinear vibration-based energy harvesters, Smart Mater. Struct. 23 (2014) 055019.
[26] B. Yang, C. Lee, W. Xiang, J. Xie, J.H. He, R.K. Kotlanka, S.P. Low, H. Feng, Electromagnetic energy harvesting from vibrations of multiple frequencies, Micromech. Microeng. 19 (2009) 035001.
[27] C.T. Saha, T. O'Donell, H. Loder, S. Beeby, J. Tudor, Optimization of an electromagnetic energy harvesting device, IEEE Trans. on Magnetics, 42(10) 2006.
[28] S.D. Moss, O.R. Payne, G.A. Hart, C. Ung, Scaling and power density metrics of electromagnetic vibration energy harvesting devices , Smart Mater. Struct. 24 (2015) 023001.
[29] Z.J. Wong, J. Yan, K. Soga, A.A. Seshia, Multi-degree-of-freedom electrostatic memspower harvester, PowerMEMS, 2009, Washington DC, USA.